

Nonequilibrium Molecular Dynamics of Microwave-Driven Zeolite–Guest Systems: Loading Dependence of Athermal Effects

Cristian Blanco[†] and Scott M. Auerbach^{*,†,‡}

Departments of Chemistry and Chemical Engineering, University of Massachusetts, Amherst, Massachusetts 01003

Received: September 10, 2002; In Final Form: December 6, 2002

We have performed molecular dynamics (MD) simulations of zeolite–guest systems driven by microwaves (MW), to study how energy is distributed in these systems as a function of guest loading. Expanding on a previously published communication [Blanco, C.; Auerbach, S. M. *J. Am. Chem. Soc.* **2002**, *124*, 6250.], we have found that MW-driven MD with the Andersen thermostat gives robust steady states, while MW-driven MD with the Nosé–Hoover chain thermostat does not. We studied MW-driven zeolites NaY, DAY and silicalite, as well as benzene and/or methanol in DAY or silicalite. DAY and silicalite exhibit little MW heating, while NaY gives strong MW heating primarily through the Na cations, whose kinetic energy was found to equilibrate on picosecond time scales. Zeolite–benzene systems show minimal MW heating, while zeolite–methanol systems exhibit significant MW heating with steady-state temperatures increasing linearly with methanol loading. MW-driven equimolar mixtures of benzene and methanol at low to medium loadings in DAY or silicalite obey $T_{\text{methanol}} \gg T_{\text{benzene}} > T_{\text{zeolite}}$, suggesting that MW heating of binary mixtures in zeolites can produce novel effects. However, MW-driven MD at higher loadings shows that $T_{\text{methanol}} \sim T_{\text{benzene}} > T_{\text{zeolite}}$, suggesting that closely related MW sorption studies can produce markedly different results viz. athermal effects.

I. Introduction

Zeolites are nanoporous crystalline aluminosilicates with a rich variety of interesting properties and industrial applications.¹ The structural and chemical versatility offered by zeolites strongly suggests that other applications lie ahead for these materials. Over the past few years, a flurry of recent interest has emerged in studying adsorption,^{2,3} ion exchange,⁴ and reaction^{5,6} in zeolites, as well as growth of zeolites^{7–9} and other oxides,^{10,11} all driven by microwave (MW) radiation.¹² For example, Turner et al.² have recently studied the effects of MW heating on a binary mixture of cyclohexane and methanol adsorbed in siliceous zeolites FAU and MFI. They found that the effect on sorption selectivity from conventional heating can be reversed by applying MW radiation. Despite this significant research activity, there remains disagreement whether MW-driven systems really behave in ways that are qualitatively different from conventionally heated systems.^{8,13,14} This disagreement is fueled, in part, by the lack of a fundamental, atomistic picture for such MW-driven systems. We seek such a fundamental picture by applying novel nonequilibrium molecular dynamics (MD) techniques to explore energy distributions in MW-driven zeolite–guest systems. In this article, we elaborate on a previously published communication¹⁵ showing that athermal energy distributions can indeed be produced in MW-driven zeolite–guest systems.

In the present work, we focus on modeling the MW-driven sorption experiments of Conner and co-workers,² in which sorption selectivities of cyclohexane–methanol mixtures in zeolites were reversed from that obtained with conventional

heating. Adsorption in porous materials is typically simulated using the grand canonical Monte Carlo approach, which assumes that the host–guest system is in thermal and chemical equilibrium with a bath of energy and guest molecules.^{16,17} Despite the fact that thermalization is rapid on the MW time scale,¹⁸ we believe that MW-driven systems must first be considered in nonequilibrium states, by the simple fact that they are driven by external fields. We therefore begin by abandoning the assumption of thermal equilibrium, thereby precluding the use of Monte Carlo methods as typically written.

The *ansatz* of our approach is to retain the concept of a temperature function. The system can deviate from thermal equilibrium by this temperature function depending upon space, time, and/or chemical identity. Such a concept is, of course, not new. Many equilibrium MD simulations track temperature as a function of time by dividing the time-dependent total kinetic energy by $dk_B/2$, where d is the (extensive) number of degrees of freedom in the system and k_B is Boltzmann's constant. For either thermostated systems or isolated systems that are sufficiently large, the temperature fluctuations so obtained are small enough to give a reasonable sampling of the canonical ensemble. However, if such a system were driven by a MW field, the corresponding MD simulation would exhibit MW heating.

Simulating the dynamics of zeolite–guest systems driven by MWs requires several approximations to yield tractable calculations. In particular, we make the classical dipole approximation for the interaction between matter and light. We further approximate that the zeolite–guest dipole moment can be represented by fixed point charges on all atoms in the system. This approximation is reasonable because of the large mismatch between MW frequencies ($\omega \sim 10^{10}–10^{12} \text{ s}^{-1}$)¹² and frequencies associated with electronic polarizabilities of silicates ($\omega \sim 10^{15} \text{ s}^{-1}$).¹⁹ Such a formulation requires force fields that attribute

* Corresponding author. E-mail: auerbach@chem.umass.edu.

[†] Department of Chemistry.

[‡] Department of Chemical Engineering.

partial charges to all atoms in the system. Toward this end, our philosophy has been to account for electrostatics regardless of whether we consider a siliceous zeolite or a cation-containing aluminosilicate.²⁰ All the force fields we have developed^{15,21–24} can thus be used within this formulation.

We show below that MW-driven MD with the Andersen thermostat gives robust steady states, while MW-driven MD with the Nosé–Hoover chain thermostat does not. We studied MW-driven zeolites NaY, DAY and silicalite, as well as benzene and/or methanol in DAY or silicalite. In general, we explore a variety of circumstances under which athermal energy distributions can be produced. We also identify mechanisms through which these athermal energy distributions might appear thermalized under certain experimental conditions.

The remainder of this article is organized as follows: Sec. II outlines the methodology we use, including a new zeolite–methanol force field. Section III provides results and discussion of MW-driven MD of bare zeolites and zeolite–guest systems, and section IV offers a summary of our findings as well as concluding remarks.

II. Methodology

Here we describe a series of molecular dynamics (MD) simulations on various zeolites and zeolite–guest systems, to determine their energy distributions when heated either with MW or with conventional heating techniques. We modeled NaY, DAY, and silicalite zeolites: three industrially important zeolites with different topologies and charge densities. We considered benzene and methanol as adsorbates: two molecules with different polarities, and hence with different dielectric permittivities. For convenience and brevity, we often refer to the systems under study as “zeolite–guest systems,” even though some of the systems we explore are bare zeolites. In what follows, we describe the basic models, potential energy functions and MD simulations studied below.

A. Zeolite–Guest Models. Zeolite NaY, an FAU-type zeolite, was chosen to represent the high-charge host. We studied NaY with a Si:Al ratio of 2.0, corresponding to a unit cell containing 128 Si and 64 Al atoms, and requiring 64 Na ions to balance charge. The Al atoms are randomly distributed within the framework while obeying Löwenstein’s empirical rule, which forbids Al–O–Al linkages. The unit cell also contains 128 O atoms bridging Si and Al atoms (denoted O_a), and 256 O atoms bridging two Si atoms (denoted O_s). As with our previously published aluminosilicate model,²¹ these oxygens have distinct properties because of their different chemical environments. Each unit cell of NaY is cubic with a lattice parameter of 24.7 Å.²⁵ In our calculations below, we explore system-size effects by performing MD on simulation cells containing one and four NaY unit cells.

Zeolite NaY contains cages separated by windows of about 7.5 Å in diameter, large enough to allow the sorption and diffusion of relatively large molecules such as xylenes and long-chain hydrocarbons.^{26,27} This microporous material is particularly interesting because many of its Na⁺ counterions show greater mobility than that of the framework atoms. Such mobility allows the system to generate significant instantaneous dipole moments, which efficiently interact with external electromagnetic fields. In fact, experimental evidence shows that MW radiation can melt NaY zeolite.^{28,29}

For the low charge limit we studied two materials with different topologies: dealuminated Y zeolite (DAY) and silicalite zeolite. We chose these two high silica zeolites because they were studied by Turner et al.² in their experiments on

competitive adsorption in MW-driven zeolites. Like NaY, DAY is a FAU-type zeolite; unlike NaY, DAY ideally has no Al in the framework and hence no Na⁺ ions to balance charge. Zeolite DAY contains 192 Si atoms and 384 O_s atoms bridging pairs of Si atoms, in a cubic unit cell with a lattice parameter of 24.3 Å.³⁰

On the other hand, silicalite is an MFI-type zeolite containing no Al or Na, just Si and O_s atoms. Silicalite has an orthorhombic unit cell with lattice parameters $a = 20.0$ Å, $b = 19.9$ Å, and $c = 13.4$ Å.³¹ In our calculations, a sufficiently large simulation box is made of $1 \times 1 \times 2$ unit cells, in the x , y , and z directions, respectively. This simulation cell has a total of 192 Si atoms and 384 O_s atoms, making it denser than DAY by a factor of ca. 1.33. Silicalite’s pore space involves straight channels intersected by zigzag channels of 5.5–5.7 Å in diameter. Small-to medium-sized molecules can diffuse through these channels, although not as freely as in DAY. In fact, it is believed that molecules such as benzene are favorably adsorbed in the channel intersections at lower loadings, whereas at higher loadings they also populate the straight and zigzag channels.³²

By using such periodic models, we may slightly underestimate the dielectric permittivities, and hence the heating rates of these materials, because our use of periodic boundary conditions ignores crystallite termination by polar silanol groups (Si–OH). In general, each zeolite simulation cell with 576 framework atoms (Si, Al and O) is denoted the basic cell. All simulations reported below were performed by fixing the simulation-cell volume and the numbers of each type of particle.

B. Potential Energy Surface. The potential energy has the following form:

$$V = V_Z + V_G + V_{ZG} + V_{GG} \quad (1)$$

where V_Z , V_G , V_{ZG} , and V_{GG} are the potential energy functions representing zeolite flexibility, guest flexibility, zeolite–guest interactions, and guest–guest intermolecular interactions, respectively. With the exception of V_G , which is taken to be a valence-bond function (vide infra), each of the potential functions involves electrostatic energies and short-range interactions. The electrostatic contribution is calculated using Ewald sums over fixed partial charges. The fixed point charge approximation is reasonable in the present context because of the large frequency mismatch between typical MW frequencies, and frequencies associated with electronic polarizabilities of oxide materials. Regarding short-range potentials, V_Z contains the Buckingham (exp-6) potential, while V_{ZG} and V_{GG} contain the Lennard-Jones (12–6) potential.

We adopt the precise form for V_Z outlined in ref 22, with framework-atom charges and other parameters reported in refs 21 and 23. We specify the remaining potential terms by setting $G = M$ and/or B for methanol or benzene, respectively. In the case where both methanol and benzene are adsorbed in the zeolite, we have that $V_G = V_B + V_M$, $V_{ZG} = V_{ZB} + V_{ZM}$, and $V_{GG} = V_{BB} + V_{MM} + V_{BM}$. In the present study, we employ the same valence-bond potential for benzene, V_B , used previously by us.²² However, we report herein a new valence-bond force field for methanol, which we describe in detail below. The zeolite–benzene interaction, V_{ZB} , is built using the form reported in ref 22, with benzene charges and Lennard-Jones parameters from ref 22, and with zeolite charges from ref 21. The Lennard-Jones parameters in V_{BB} and V_{MM} are taken from the CVFF force field;³³ those in V_{BM} are derived using the Lorentz–Berthelot mixing rules.¹⁶ We are thus left to determine the partial

TABLE 1: Partial Charges for Methanol

species	partial charge
H ^a	+0.225
O	-0.431
C	+0.021
H ^b	+0.062

^a Hydroxyl hydrogen. ^b Average over all methyl hydrogen charges.

TABLE 2: Intramolecular Potential Parameters for Methanol

Quadratic Bond: $1/2K_b(r - r_0)^2$			
bond	K_b (eV/Å ²)	r_0 (Å)	
O-H	45.38	0.945	
C-O	34.32	1.425	
C-H	27.80	1.094	
Quadratic Angle: $1/2K_a(\theta - \theta_0)^2$			
angle	K_a (eV/rad ²)	θ_0 (degrees)	
C-O-H	5.60	108.32	
H-C-O	5.50	106.90	
H-C-H	4.40	108.38	
Torsion Angle: $K_t(1 + \alpha \cos \beta \phi)$			
torsion	K_t (meV)	α	β
H-C-O-H	7.62	+1.0	3.0

charges on methanol for calculating V_{ZM} , V_{MM} , and V_{BM} , the short-range parameters for V_{ZM} , and the valence-bond parameters for V_M .

1. Partial Charges. In addition to playing an important role in determining potential energies in our zeolite-guest model, the electric charge distribution also controls energy transfer from the MW field (vide infra).³⁴ Because we model the charge distribution via fixed point charges, we must take care in choosing these partial charges. As discussed above, the benzene²² and zeolite²¹ partial charges are taken from previous publications. The benzene charges were extracted from MNDO calculations of Bull et al.;³⁵ the zeolite charges were fitted to infrared (IR) spectra by analyzing dipole autocorrelation functions.²¹ Although a variety of partial charge sets for methanol can be found in the literature,^{32,36,37} dipole moments computed with these charge sets differ from the experimental value of 1.71 D.^{37,38} To model more accurately the charge distribution of methanol, we performed electronic structure calculations to estimate its partial charges as well as other structural parameters.

Table 1 shows methanol's partial charges obtained by performing *ab initio* calculations at the QCISD level of theory using the 6-311++G(2d,2p) basis set, which is accessible within the GAUSSIAN98 program suite.³⁹ This combination of basis set and level of theory is sufficient to converge methanol's ground-state energy, geometry and charge distribution to reasonable accuracy. The partial charges in Table 1 were extracted by Mulliken population analysis.⁴⁰ Although the results of this procedure can depend on the basis set, we found that the charges are reasonably insensitive to changes in the basis set as long as it is sufficiently complete. To check the validity of the new partial charge set we computed methanol's average dipole moment from a gas-phase MD simulation, finding 1.71 ± 0.06 D, in remarkably good agreement with the experimental value. We also tested methanol's partial charges by comparing the simulated IR spectrum (Fourier transform of the gas-phase dipole autocorrelation function) with the corresponding experimental IR spectrum, finding good agreement.^{37,41} The computed IR spectrum, as well as a report comparing simulated and

TABLE 3: Zeolite-Methanol Lennard-Jones Parameters

species	ϵ_{ij} (meV)	σ_{ij} (Å)
O-H ^a	5.116	3.006
O-O	5.820	3.665
O-C	5.906	3.840
O-H ^b	3.878	3.325

^a Hydroxo hydrogen in methanol. ^b Methyl hydrogen in methanol.

experimental structural data for methanol, are summarized in the Supporting Information.

2. Short-Range Parameters. We now discuss construction of V_M and the short-range portion of V_{ZM} . Whereas zeolite flexibility, zeolite-guest, and guest-guest interactions are modeled almost exclusively via through-space, two-body interactions, guest molecule flexibility is described with two-body bond stretches, three-body angle bends, and four-body torsional potentials. A particularly important torsional mode, for example, is methanol's hindered rotation, which is due to the hydroxo-hydrogen spinning around the C-O axis.^{38,41,42} For consistency with our valence-bond model of benzene, we assume that V_M takes the form:

$$V_M = \sum_{\text{bonds}} \frac{1}{2} K_b (r - r_0)^2 + \sum_{\text{angles}} K_a (\theta - \theta_0)^2 + \sum_{\text{torsions}} K_t (1 + \alpha \cos \beta \phi) \quad (2)$$

Parameters were obtained by fitting to our own *ab initio* data, to millimeter-wave spectroscopy^{38,43} and to electron diffraction data⁴² for methanol. The resulting parameters are shown in Table 2. We checked the accuracy of the new potential by comparing the simulated IR spectrum with methanol's gas-phase IR spectrum,^{37,41} finding extremely good agreement.

The zeolite-methanol interaction potential V_{ZM} takes the following standard form:

$$V_{ZM} = \sum_{i \in Z} \sum_{j \in M} \left\{ \frac{q_i q_j}{r_{ij}} + 4 \epsilon_{ij} \left[\left(\frac{\sigma_{ij}}{r_{ij}} \right)^{12} - \left(\frac{\sigma_{ij}}{r_{ij}} \right)^6 \right] \right\} \quad (3)$$

where q_i and q_j are the partial charges on zeolite and methanol atoms, respectively, and $\{\epsilon_{ij}, \sigma_{ij}\}$ are the Lennard-Jones parameters. Initial values of $\{\epsilon_{ij}, \sigma_{ij}\}$ were obtained from the CVFF force field;³³ these values were adjusted by trial-and-error to fit heats of adsorption⁴⁴⁻⁴⁷ and diffusion constants^{26,48} of methanol in DAY and silicalite. The resulting values of $\{\epsilon_{ij}, \sigma_{ij}\}$ for zeolite-methanol interactions are shown in Table 3.

C. MD Simulations. All MD simulations were performed with our in-house program DIZZY.⁴⁹ In all cases, all atoms in the simulation were allowed to evolve dynamically during the entire MD run. Periodic boundary conditions were enforced via the minimum image convention.¹⁶ Short-range interactions were cutoff and shifted at either 9 or 12 Å, when modeling MFI- or FAU-type zeolites, respectively. All MD simulations were initiated from energy-minimized zeolite-guest structures, which were obtained by our simulated annealing procedure called MD-DOCKER.^{22,23} Such an initial condition allows us to target particular temperatures with or without a thermostat (vide infra), by exploiting the nearly harmonic nature of zeolite-guest systems. Indeed, nearly half the initial kinetic energy pools into potential energy, on average.

We employed the velocity Verlet algorithm to integrate Newton's equations with a time step of 1 fs. Total simulation times were at least 100 ps, and often considerably longer. A

100 ps MD simulation of a system containing ca. 700 particles (one unit cell) required 72 CPU hours (3 CPU days) on a 1 GHz Pentium III processor running Linux with 512 MB RAM. A corresponding MD simulation with four unit cells required 18 CPU days on the same machine, indicating a mildly supra-linear scaling of CPU time with system size.

To simulate the dynamics of zeolite–guest systems driven by MWs, we make the classical dipole approximation for the interaction between matter and light. That is, the zeolite–guest Hamiltonian is augmented by a term of the form $\vec{\mu}_i \cdot \vec{E}_i$, where $\vec{\mu}_i$ is the time-dependent zeolite–guest dipole moment, and \vec{E}_i is the MW electric field. We assume that the MW field points along the z -axis, and is homogeneous in space because its wavelength is huge compared to typical MD length scales. We consider a monochromatic electric field of the form $\vec{E}_i = E \cdot \hat{z} \cdot [\cos(\omega t)]$, where E is the MW field strength and ω is the MW frequency. As discussed above, we further approximate that the zeolite–guest dipole moment can be represented by fixed point charges on all atoms in the system.

Given these approximations, Hamilton’s equations of motion become:

$$\frac{d\vec{r}_i}{dt} = \frac{\vec{p}_i}{m_i} \quad \frac{d\vec{p}_i}{dt} = -\frac{\partial V}{\partial \vec{r}_i} + q_i \cdot \vec{E} \quad (4)$$

where \vec{r}_i and \vec{p}_i are the three-dimensional position and momentum of particle i , respectively, m_i and q_i are its mass and charge, and $V = V(\vec{r}_1, \vec{r}_2, \dots, \vec{r}_N)$ is the zeolite–guest potential energy function described above. The additional electrostatic force in eq 4, namely, $q_i \cdot \vec{E}_i$, attempts to push charged particles to the left or right along the z -axis, depending upon the sign of the charge and the phase of the electric field. Such forces can excite vibrations of zeolite atoms, vibrations, and translations of exchangeable cations in a zeolite, and of course, the field can excite external vibrations and librations of guest molecules in zeolites.

Various values of the MW field strength were considered: Bare zeolites (NaY, silicalite and DAY) were exposed to field strengths in the ranges 0.10–0.45, 0.1–1.8, and 0.1–2.4 V/Å, respectively. In each case, the upper limit indicates the value at which the system undergoes uncontrollable runaway heating. As expected, the trend: $E_{\max}(\text{NaY}) < E_{\max}(\text{silicalite}) < E_{\max}(\text{DAY})$ anticorrelates with the dielectric permittivities measured experimentally for these zeolites.^{2,29} For consistency, the field strength was set to 1.5 V/Å for all MD simulations of guests adsorbed in siliceous zeolites. We set ω to three values that fall in the blue end of the MW spectrum, namely, 9.4×10^{10} , 9.4×10^{11} , and $9.4 \times 10^{12} \text{ s}^{-1}$, to explore how changing the MW frequency influences the dynamical properties of MW-driven zeolite–guest systems.

To compare with experiments under steady-state conditions, which are produced by using a carrier gas such as He,^{2,3} we introduced a thermostat to simulate the cooling that occurs when carrier gas particles collide with MW-heated zeolite–guest particles on the inflow side. Initially, we used the Nosé–Hoover chain approach of Martyna et al.^{50–52} implemented according to Jang and Voth^{53,54} with a chain of four thermostats. Surprisingly, as we show below, we could not find thermostat parameters that produce robust steady states. For a remarkably broad range of thermostat masses, we observed no MW heating at all. When we adjusted the Nosé–Hoover chain parameters to produce milder thermostats, the system exhibited marked instability. We postulate that this behavior arises because the Nosé–Hoover thermostat influences all atoms at each step.

We then applied a thermostat based on the model of Bohm and Gross,^{55,56} subsequently popularized by Andersen.⁵⁷ This approach, now known as the Andersen thermostat, replaces the three-dimensional velocities of randomly selected atoms at random times, with those from appropriate Maxwell–Boltzmann distributions. These replacements model the effect of collisions assuming instantaneous energy transfer with carrier gas particles. The velocity replacements of different particles are assumed to be uncorrelated, occurring at random times chosen from a Poisson distribution. We implemented Andersen’s thermostat in DIZZY by specifying two parameters in addition to the target temperature: τ , the average time between velocity replacements, and n , the number of particles influenced at each replacement. With regard to this latter parameter, we note that in contrast with the Nosé–Hoover approach, the Andersen thermostat allows explicit control over the number of particles influenced at each time step. In practice, the ratio of Andersen parameters τ/n is sufficient to distinguish one Andersen thermostat from another.

As we show below, the Andersen thermostat yields steady states that are reasonably robust to changes in thermostat parameters. While stochastic velocity-replacement likely reflects the microscopic dynamics of cooling in this system, the final steady states we obtain do depend on the nature of the thermostat. To explore this issue more fully, we plan in future work to consider other thermostats, explicit He collisions, and the relevant energy balances between system and thermostat.

To explore how changing the system influences MW heating properties, we define a time-dependent system temperature $\langle T(t) \rangle$ obtained by properly normalizing the total system kinetic energy at each MD time step. $\langle T(t) \rangle$ can be calculated with or without the perturbations of the field and the thermostat. To distinguish between energy distributions in equilibrium systems from those in MW-driven, steady-state systems, we also define steady-state temperatures for each atom type in the system, denoted $T_{\text{ss}}(i)$, where i labels the atom type. These were obtained by exploiting the empirical fact from our computer simulations that, even in the MW-driven MD (MWMD) simulations, all velocity distributions remained Gaussian. We thus extracted effective temperatures for each atom type by appropriately normalizing the steady-state kinetic energy summed over all atoms of a given type. A system was deemed to be thermal when all atom types have the same temperature within statistical precision; athermal systems are those where different atom types exhibit statistically different temperatures.

To avoid unphysical energy drifts during MWMD simulations, we equilibrated the system for 5 ps before applying the MW field. The thermostat temperature for all thermostated simulations was set to 300 K.

III. Results and Discussion

We performed equilibrium MD (EMD) and MWMD simulations of bare zeolites, of single-component guest phases in zeolites, and of binary mixtures in zeolites. We begin by discussing EMD and MWMD simulations of bare NaY, DAY and silicalite. We then introduce Andersen’s thermostat to model steady states in these zeolites; below we detail the results for NaY. We then discuss simulations of either benzene or methanol adsorbed in DAY or silicalite; we considered loadings of 1, 2, 4, 8, and 16 molecules per basic cell for each zeolite–guest system. Finally, we study equimolar mixtures of methanol and benzene in DAY and in silicalite, considering loadings of 1:1, 2:2, 4:4, 8:8, and 16:16 molecules of benzene:methanol per basic cell of DAY and silicalite. From these simulations, we determine

the MW field effect by comparing thermal energy distributions to those at steady state, and by simulating the relaxation dynamics from steady state to equilibrium.

A. Equilibrium MD. We performed EMD simulations on most of the zeolite–guest systems studied below to establish baselines of equilibrium behavior, and also to explore the accuracy of the new zeolite–methanol force field detailed above. Regarding the latter, we calculated MD-averaged energies of methanol adsorption in both DAY and silicalite, as functions of methanol loading for comparison with experimental heats.^{45,47} For a simulation cell with n guest molecules adsorbed, the constant-volume molar adsorption energy $\Delta\bar{U}_{\text{ads}}$ is given by

$$\Delta\bar{U}_{\text{ads}} = [\langle V_{z+g} \rangle - (\langle V_z \rangle + n\langle V_g \rangle)]/n \quad (5)$$

where $\langle V_{z+g} \rangle$, $\langle V_z \rangle$, and $\langle V_g \rangle$ are the average potential energies of the zeolite–guest system, the bare zeolite, and the gas-phase guest, respectively, all averaged at the same temperature. For comparison with constant-pressure adsorption heats, we require the molar adsorption enthalpy, $\Delta\bar{H}_{\text{ads}} = \Delta\bar{U}_{\text{ads}} + \Delta(p\bar{V})_{\text{ads}}$, which we estimate by ignoring the partial molar volume of the adsorbed phase, and by assuming that the external methanol vapor is ideal. These approximations give: $\Delta\bar{H}_{\text{ads}} \cong \Delta\bar{U}_{\text{ads}} - RT$. The constant-pressure heat of adsorption q_{ads} is simply the negative of $\Delta\bar{H}_{\text{ads}}$.

To facilitate detailed comparisons with experimental heats at 300 K, we fitted the loading dependence of q_{ads} (kJ mol⁻¹) to a first-order virial expansion in the density of adsorbed methanol, ρ (mmol methanol per gram zeolite), according to $q_{\text{ads}} = q_{\text{ads}}^{(0)} + b\rho$. For methanol in silicalite, Thamm reported $q_{\text{ads}}^{(0)} = 43$ kJ mol⁻¹ and $b = 4.0$,⁴⁵ whereas our 300 K simulations give $q_{\text{ads}}^{(0)} = 42.4$ kJ mol⁻¹ and $b = 4.3$, in quite good agreement. For methanol in DAY, Izmilova et al. reported $q_{\text{ads}}^{(0)} = 45$ kJ mol⁻¹ and $b = 0.05$,⁴⁷ indicating a very flat loading dependence, which is perhaps not surprising in the larger pores of FAU-type zeolites. Our simulations give $q_{\text{ads}}^{(0)} = 40.0$ kJ mol⁻¹ and $b = -0.47$, thereby underestimating the zero-loading heat by about 11%. In qualitative agreement with experiment, we predict a rather flat loading dependence for q_{ads} ; however, while Izmilova et al. find that q_{ads} increases slowly with loading, we find that q_{ads} decreases slowly with loading. The discrepancy in the sign of b for methanol in DAY is rather small, amounting to only a couple kJ mol⁻¹ for the loadings we consider. We thus find reasonable agreement between simulated and experimental adsorption heats for methanol in silicalite and DAY zeolites.

The comparisons above test the new force field's ability to reproduce the balance between zeolite–methanol and methanol–methanol interactions at stable binding sites. To benchmark the new force field's performance away from stable binding sites, we have calculated the temperature dependencies of methanol self-diffusion coefficients in DAY and silicalite. Unfortunately, we could not find experimental activation energies for comparison. To prompt new self-diffusion measurements, we report our calculated activation energies: $E_{\text{act}} = 13.9$ and 18.4 kJ mol⁻¹ for methanol in DAY and silicalite, respectively.

B. MWMD of Bare Zeolites. In Figure 1 we show the time-dependent temperature $\langle T(t) \rangle$ for the three different zeolites under various field strengths, in all cases without a thermostat. We observe that two distinct heating regimes can be identified: linear heating for weak fields and exponential heating for strong fields. The former is characteristic of the siliceous zeolites over a large range of external field strengths. The presence of Na cations in Na–Y zeolite produces strong coupling with the

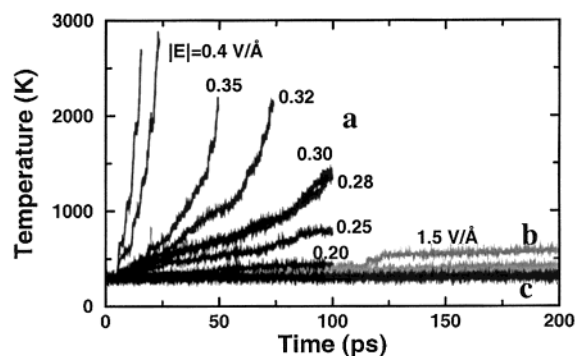


Figure 1. Heating of bare zeolites with different MW strengths, using MW frequency 9.4×10^{11} s⁻¹: (a) NaY, (b) silicalite, and (c) DAY.

external field, due mainly to the higher mobility of the ions compared with that of the framework atoms, which allows larger fluctuations of the instantaneous dipole moment distributed throughout the zeolite. This is consistent with the runaway conditions observed experimentally when applying MWs to zeolites without using a carrier gas.^{28,29} To test whether these runaway-heating patterns result from unstable integration of Newton's equation at high temperatures, we ran additional simulations with smaller time steps (data not shown) finding essentially the same heating patterns as in Figure 1. As a further check of the integrator, we performed EMD simulations of Na–Y at 2000 K with a 1 fs time step. Even at this high temperature the integrator gives very good energy conservation. These results show that the heating patterns in Figure 1 do not result from unstable integration, but rather from the absorption of microwave energy.

Statistical analysis and molecular graphics provide insights into the different microscopic motions that produce linear and exponential heating. In particular, the linear heating regime is characteristic of Na vibrations being excited, while exponential heating occurs when Na translations become significant. These two heating regimes are thus characterized by *qualitatively different* mean square displacements for Na cations (data not shown), even when these two regimes *overlap significantly* in temperature. It is possible that while some experimentalists sample the linear regime, others sample the exponential regime, suggesting why there is a difference of opinion over whether MWs can strongly influence zeolite systems.

Our simulations predict that DAY and silicalite exhibit relatively slow MW heating. As discussed above, we may underestimate the heating rates of these materials, because our use of periodic boundary conditions ignores crystallite termination by polar silanol groups (Si–OH). Nonetheless, for a given MW field strength and heating time, we predict the trend $T_{\text{NaY}} \gg T_{\text{silicalite}} > T_{\text{DAY}}$, which agrees qualitatively with experiment.² The fact that silicalite heats more rapidly than does DAY correlates well with their relative densities.

In other simulations (data not shown), we explored how changing the MW frequency influences heating rates in NaY, DAY and silicalite. For a given field strength, we found that NaY heats more rapidly and more strongly when increasing the MW frequency. For example, the MW field strength where linear heating changes to exponential heating is in the range 0.25–0.30 V/Å for $\omega = 9.4 \times 10^{11}$ s⁻¹. Increasing the MW frequency by a factor of 10 decreases this transition field strength to 0.1–0.2 V/Å. We also found that by increasing ω to 9.4×10^{12} s⁻¹, DAY and silicalite exhibited the linear to exponential heating transition for MW fields in the range 1.0–2.0 V/Å. Because of the simplicity of our model for energy absorption and zeolite charge distributions, these results merely predict

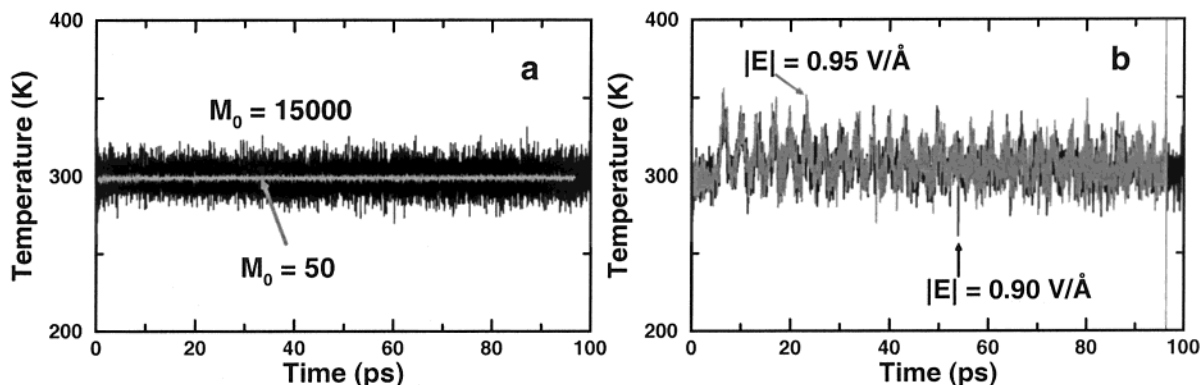


Figure 2. MWMD simulations of NaY with the Nosé–Hoover thermostat. (a) Results from thermostat masses $M_0 = 50$ and 15000 amu with MW $E = 0.45$ V/Å: no MW heating is observed. (b) Results from MW $E = 0.90$ and 0.95 V/Å with $M_0 = 15000$ amu: gives dynamical instability.

qualitative trends, not quantitative details. Because most MW experiments fix the frequency and vary power, we fix the MW frequency at $\omega = 9.4 \times 10^{11}$ s $^{-1}$ for all the calculations reported below.

C. Thermostated MWMD of NaY. To model steady-state zeolite–guest systems heated by MWs and cooled by a carrier gas, we performed thermostated MWMD simulations. Figure 2a,b summarize our findings with the Nosé–Hoover chain thermostat by plotting the temperature of NaY as a function of time. The two simulations shown in Figure 2a involve $E = 0.45$ V/Å, the field strength that produces the most rapid runaway heating in Figure 1. Figure 2a shows that no MW heating is observed for a remarkably wide range of masses M_0 of the first Nosé–Hoover chain particle, from $M_0 = 50$ to 15000 amu. As expected, we do see temperature fluctuations increase over this range from $\langle T \rangle = 299.0 \pm 0.2$ K to 299.5 ± 8.2 K, respectively, but no heating is seen. The temperature fluctuations in Figure 2a are comparable to those obtained without the MW field (data not shown). For this range of thermostat masses, the Nosé–Hoover chain thermostat is clearly dominating over this MW field. We found that larger values of M_0 (e.g., 20000 amu) give rise to unstable trajectories.

To force the issue, we increased the MW field strength to 0.90 – 0.95 V/Å and set the first Nosé–Hoover chain mass to $M_0 = 15,000$ amu. The resulting temperature profiles are shown in Figure 2b. When $E = 0.90$ V/Å, the system is clearly driven by both the field and the thermostat. However, the temperature statistics during the run, $\langle T \rangle = 306.7 \pm 12.4$ K, indicate that even for this extremely strong field, no net MW heating has occurred. When increasing the field strength to $E = 0.95$ V/Å, the simulation became unstable before 100 ps as shown in Figure 2b. These results prompted us to explore the properties of other thermostats.

The temperature profiles resulting from MWMD with the Andersen thermostat are shown in Figure 3. These simulations fixed $E = 0.3$ V/Å, while the Andersen parameter τ/n (fs/particle) was varied over the range 0.5 to ∞ , with lower values of τ/n giving stronger thermostats. Indeed, profile (a) in Figure 3 shows that MWMD with $\tau/n = 0.5$ fs/particle yields no MW heating, with temperature statistics of $\langle T \rangle = 301.1 \pm 7.3$ K. Obviously, $\tau/n = \infty$ means no thermostat at all; runaway heating is thus observed in profile (e). Intermediate values of $\tau/n = 7$, 10, and 12 fs/particle give steady states as shown in profiles (b), (c), and (d), respectively, with temperature statistics of 395.8 ± 25.5 , 412.4 ± 14.4 , and 390.6 ± 22.3 K. These three steady states involve “temperatures” that are statistically identical, indicating that (as advertised above) the Andersen thermostat yields steady states that are reasonably robust to changes in

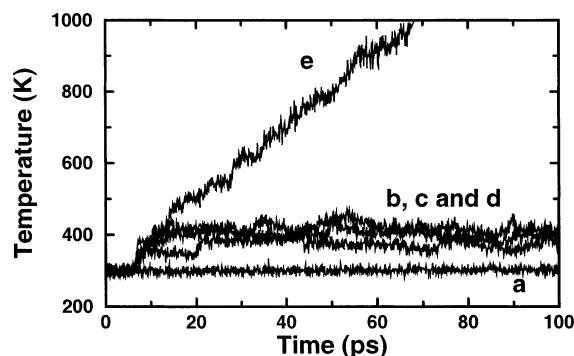


Figure 3. MWMD simulations of NaY with the Andersen thermostat, using τ/n (fs/particle) values of: (a) 0.5, (b) 7, (c) 10, (d) 12, and (e) ∞ .

thermostat parameters. Most of the simulations reported below involve replacing the three-dimensional velocity of one atom every 10 fs (on average), corresponding to replacing all velocities approximately every 7 ps (on average). While stochastic velocity-replacement likely reflects the microscopic dynamics of cooling in this system, the final steady states we obtain do depend on the nature of the thermostat. To explore this issue more fully, we plan in future work to consider other thermostats, explicit He collisions, and the relevant energy balances between system and thermostat.

We have found that the steady states displayed in Figure 3 are dynamically stable for rather long times, much longer than 100 ps. Despite their stability, the temperature fluctuations in Figure 3 appear relatively large. To determine the extent to which the size of our simulation cell influences steady-state temperature fluctuations, we performed thermostated MWMD of NaY comparing temperature profiles from simulation cells containing $1 = 1^3$ and $4 = 2^3/2$ basic cells. The thermostat parameter in these simulations, shown in Figure 4, is $\tau/n = 7$ fs/particle; while the MW strengths are (a) $E = 0.30$ V/Å and (b) $E = 0.25$ V/Å. The gray and black profiles were calculated using 1 and 4 basic cells, respectively. These simulations show two expected and reassuring qualitative trends. First, the average steady-state temperature increases with MW field strength. Second, for a given field strength, the distribution of temperatures narrows with increasing system size. We thus expect macroscopic systems to display essentially constant steady-state temperature profiles; that is precisely what is observed experimentally by Turner et al. in Figures 4 and 5 of ref 2.

Quantitatively, the temperature statistics from profiles (a) are $\langle T \rangle = 372.8 \pm 17.7$ and 377.1 ± 9.2 K for 1 and 4 basic cells, respectively; likewise for (b) we obtain $\langle T \rangle = 317.1 \pm 13.8$ and 319.2 ± 4.9 K. These results suggest that, although the

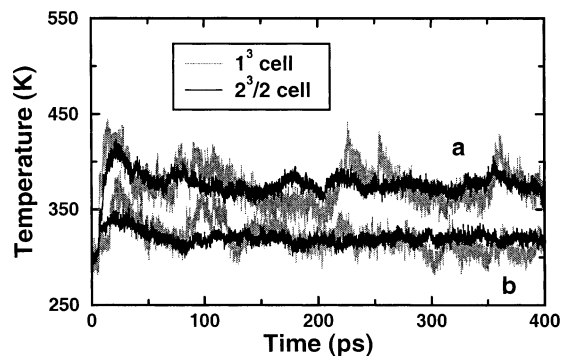


Figure 4. Dependence of steady-state temperature fluctuations with system size for NaY using $\tau/n = 7$ fs/particle, with (a) $E = 0.30$ V/Å, and (b) $E = 0.25$ V/Å.

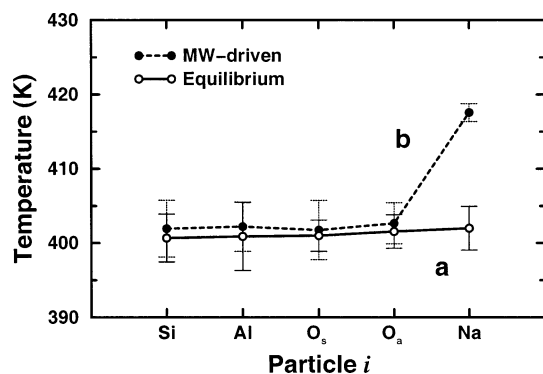


Figure 5. Energy distributions in NaY at (a) thermal equilibrium (400 K) and (b) MW-driven steady state with $E = 0.30$ V/Å and $\tau/n = 10$ fs/particle. O_a and O_s are oxygen atoms bridging Si and Al atoms, and two Si atoms, respectively.

temperature dispersions vary with system size, the average steady-state temperatures are statistically independent of system size for the sizes we consider here. Based on these results, the calculations reported below are based, for computational efficiency, on single basic cells for all materials studied.

With no MW field we simulate equilibrium states, whereas with both MWs and the thermostat we simulate steady states. Here we address the question of whether such systems, with both equilibrium and steady-state temperatures, have qualitatively similar energy distributions. These energy distributions are shown in Figure 5 for NaY at ca. 400 K. At equilibrium, all atoms in the system are at the same temperature, as expected. In contrast, when NaY is exposed to MW energy, the effective steady-state temperature of Na atoms is considerably higher than that for the rest of the framework, indicating an athermal energy distribution. This athermal effect arises because, even though the Na ions continuously dissipate energy into the framework, the dissipation is not efficient enough in our simulations to completely thermalize the absorbed energy.

The persistence of an athermal energy distribution in Figure 5 prompted us to determine the rate of energy dissipation from the Na cations to the NaY framework. Although the precise values of such energy transfer rates can depend on the initial Na and framework steady-state temperatures, and hence on the MW and thermostat parameters, here we seek a typical order of magnitude. To obtain this, we prepared several macroscopically identical but microscopically independent steady states such as that shown in Figure 5, except with $E = 0.4$ V/Å. We then evolved these systems with the MW field and thermostat both turned off, to observe the unperturbed relaxation dynamics. We turned the thermostat off because we wanted to avoid the possibility of contaminating the Na dynamics by the Andersen

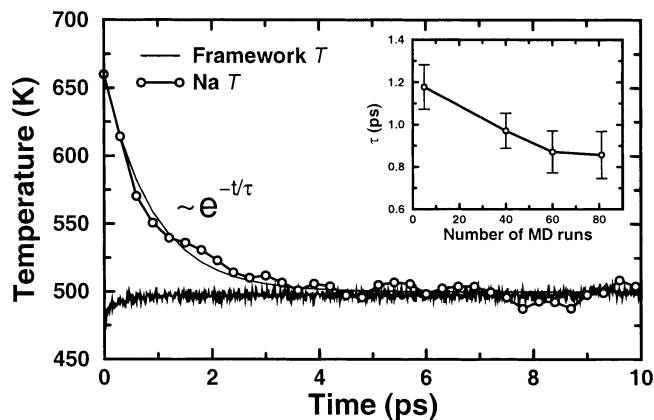


Figure 6. Relaxation of effective Na temperature from MW-driven steady states, initially prepared using $E = 0.4$ V/Å and $\tau/n = 10$ fs/particle. Inset shows convergence of the exponential decay constant vs the number of MD runs.

thermostat. In previous work, we have shown that the zeolite framework serves as an excellent natural heat bath in standard NVE dynamics.⁵⁸ We then recorded the total kinetic energy of the Na atoms as a function of time. When properly normalized this yields a time-dependent effective Na temperature, which we averaged over the independent MD runs.

As an aside, we note that this process is formally similar to the *gedanken* experiment underlying the standard fluctuation–dissipation theorem,⁵⁹ except for one important distinction. The standard derivation of the fluctuation–dissipation theorem considers the average relaxation from an equilibrium state of a perturbed Hamiltonian, to another equilibrium state of an unperturbed Hamiltonian.⁵⁹ Like the Na dynamics we study below, relaxation treated by the fluctuation–dissipation theorem arises from turning off a perturbation. However, unlike the standard fluctuation–dissipation theorem, we consider equilibration from a nonequilibrium steady state. It remains an interesting and technologically important field of statistical physics to characterize relaxation from steady states by appropriately generalizing the fluctuation–dissipation theorem; see, e.g., refs 60–64.

Figure 6 shows the decay of the effective Na temperature, obtained by averaging the relaxation of 80 independent MD simulations. The temperature decay can be fitted to a single exponential; we constrain the fit to agree with the initial temperature extracted from the steady-state analysis (cf. Figure 5). The convergence of the exponential decay time constant, with respect to the number of averaged MD runs, is shown inset in Figure 6. The converged time constant is found to be approximately 0.85 ps, which translates to about 40 cm^{-1} . This falls below the populated regions ($100 \text{ cm}^{-1} < \bar{\nu} < 300 \text{ cm}^{-1}$) of the vibrational densities of states (VDOS) for Na cations in NaY, calculated previously by Jaramillo and Auerbach using the present force field.²¹ However, these previous VDOS calculations were performed with the Y framework held fixed, which tends to blue-shift cation vibrations.⁵⁸ As such, we performed new VDOS calculations for the present study allowing for Y framework flexibility. For various Na cation locations in NaY (data not shown), we found that the red ends of the VDOSs do indeed move to lower wavenumbers when allowing the framework to flex, but none moves as low as 40 cm^{-1} . Because the VDOS provides information about local, single-particle vibrations, these results suggest that the Na relaxation observed above is controlled by collective motions of strongly coupled Na atoms. If indeed this is so, it remains surprising that the relaxation can be fitted to a single exponential.

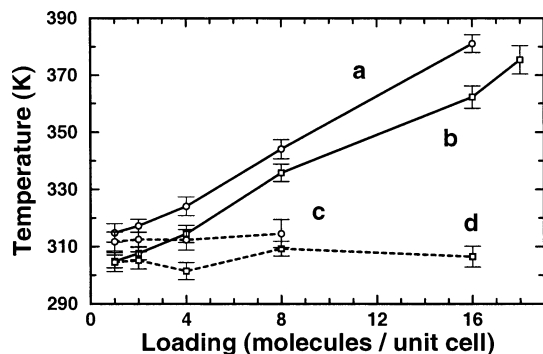


Figure 7. Loading dependence of steady-state temperatures from MWMD of (a) methanol in silicalite, (b) methanol in DAY, (c) benzene in silicalite, and (d) benzene in DAY. All simulations were performed with $E = 1.5 \text{ V/\AA}$ and $\tau/n = 10 \text{ fs/particle}$.

In future work, we will explore how relaxation dynamics in MW-driven zeolite–guest systems are influenced by cation-frame, zeolite–guest and guest–guest energy transfer processes.

As a practical matter, we note that MW radiation is often applied with a “duty cycle” to avoid overheating, where the field is cycled back and forth between being on for some time, and off for another time. If the off-time is comparable to or longer than the equilibration time, which is 0.85 ps for the case above, then the system will have ample opportunity to equilibrate after each new steady state is created, producing the appearance of conventional heating. This may provide another clue why some researchers find no athermal behavior from MW-driven zeolites.

D. Zeolite–Guest MWMD with Benzene or Methanol.

Having now predicted that nonequilibrium energy distributions can be created in bare, MW-driven zeolites, we now explore the behavior of MW-driven zeolite–guest systems. We first consider single-component adsorbed phases of either benzene or methanol in the siliceous zeolites, DAY, or silicalite. In each of the four resulting zeolite–guest systems, we apply a MW field with $E = 1.5 \text{ V/\AA}$ and a thermostat with $\tau/n = 10 \text{ fs/particle}$. As found previously (cf. Figure 1), the siliceous zeolites do not exhibit appreciable MW heating. However, the guest phases present another story.

We show in Figure 7 the steady-state, total system temperatures of methanol (a,b) and benzene (c,d) in DAY and silicalite as a function of guest loading. Several qualitative findings are observed. First, the zeolite–benzene systems do not show much MW heating, because benzene lacks a permanent dipole moment in its gas-phase equilibrium geometry. On the other hand, the zeolite–methanol systems do exhibit significant MW heating because of methanol’s permanent dipole moment (1.71 D).³⁸ Second, the extent of MW-heating in the zeolite–methanol systems is roughly proportional to the loading of methanol, because increasing this loading increases the density of dipolar absorbers in the system. The temperatures in Figure 7a,b reflect an average over zeolite temperatures (300–350 K) and methanol temperatures (450–550 K). Third, the MW heating results are roughly independent of the framework type between FAU- and MFI-type zeolites, presumably because of the lack of special adsorption sites in either system.

Overall, these results establish the fact that MW-driven zeolite–guest systems can be maintained at different temperatures of zeolite and guest phases. As with the NaY case, this can be rationalized based on inefficient energy transfer between zeolite and guest, presumably because of the frequency mismatch between zeolite framework vibrations ($500\text{--}1200 \text{ cm}^{-1}$)^{65,66} and guest molecule external vibrations ($50\text{--}100 \text{ cm}^{-1}$).^{58,67}

However, a binary mixture might exhibit efficient energy transfer between the guests, suggesting that it might be unlikely to maintain different guests at different steady-state temperatures.

E. Zeolite–Guest MWMD with Benzene and Methanol.

To address this issue, we modeled several loadings of methanol–benzene equimolar mixtures in DAY and silicalite. To ensure that the results for each loading are statistically reliable, we performed several independent runs from very different initial guest configurations. Results were accepted only if various runs gave qualitatively identical energy distributions; error bars were extracted from the various independent runs assuming a 95% confidence interval. In Figure 8a,b we detail results for DAY zeolite; qualitatively similar results were obtained for binary mixtures in silicalite (data discussed below but not shown). For comparison, both Figure 8a,b show equilibrium results (16:16-eq) for 16:16 benzene:methanol molecules per basic cell. In both Figure 8a,b, $n:n$ -mw indicates MWMD results for $n:n$ benzene:methanol per basic cell. The regions in the graph represent (from left to right) zeolite atoms, benzene atoms, methanol atoms, and centers-of-mass of benzene and methanol, respectively.

For loadings of 1:1 and 4:4 benzene:methanol per basic cell, Figure 8a shows statistically different temperatures for each component satisfying $T_{\text{methanol}} \gg T_{\text{benzene}} > T_{\text{zeolite}}$. At these low loadings, methanol dissipates energy to benzene too inefficiently to thermalize the system. Figure 8b shows that different steady-state temperatures can be maintained even for a loading of 8:8 benzene:methanol per basic cell. This result is remarkable because at this loading, each DAY cage is filled (on average) with one benzene and one methanol, suggesting the possibility of thermalization through such proximity. However, such thermalization is not seen.

Increasing the loading to 16:16 benzene:methanol per basic cell produces a system with an average of two benzenes and two methanols per DAY cage; these MWMD temperatures are shown in Figure 8b 16:16-mw. Although this system is clearly not at equilibrium, energy transfer between the benzene and methanol phases is much more efficient, as evidenced by the statistical equivalence of their center-of-mass temperatures, B_{COM} and M_{COM} in Figure 8b, respectively. Figure 8b 16:16-mw also provides the first example of overlap between the atomic temperatures of benzene and methanol, another signal of enhanced energy transfer. The steady-state temperatures of the 16:16-mw case satisfy $T_{\text{methanol}} \sim T_{\text{benzene}} > T_{\text{zeolite}}$. The sensitivity of these energy distributions on guest loading may suggest yet another reason some researchers find interesting MW effects while others do not.

Qualitatively similar results were obtained for energy distributions of MW-driven benzene–methanol mixtures in silicalite, as a function of guest loading (all with $E = 1.5 \text{ V/\AA}$ and $\tau/n = 10 \text{ fs/particle}$). This concurrence might seem surprising when considering the very different framework structures of FAU- and MFI-type zeolites. To explain this, we recall that our silicalite simulation cell is comprised of two silicalite unit cells, each of which contains four channel intersections, thus totaling eight intersections in the simulation cell. Our MW-driven MD simulations of 1:1, 2:2, 4:4, and 8:8 benzene:methanol in silicalite generally involve benzenes in intersections and methanols in channels, in agreement with other adsorption simulations showing that benzene occupies MFI intersections when possible.³² This partitioning makes energy transfer between the benzene and methanol phases very inefficient. These loadings thus sustain strong MW-driven athermal energy distributions, with typical center-of-mass temperatures of 370 ± 15 and $440 \pm 15 \text{ K}$ for benzene and methanol, respectively. However,

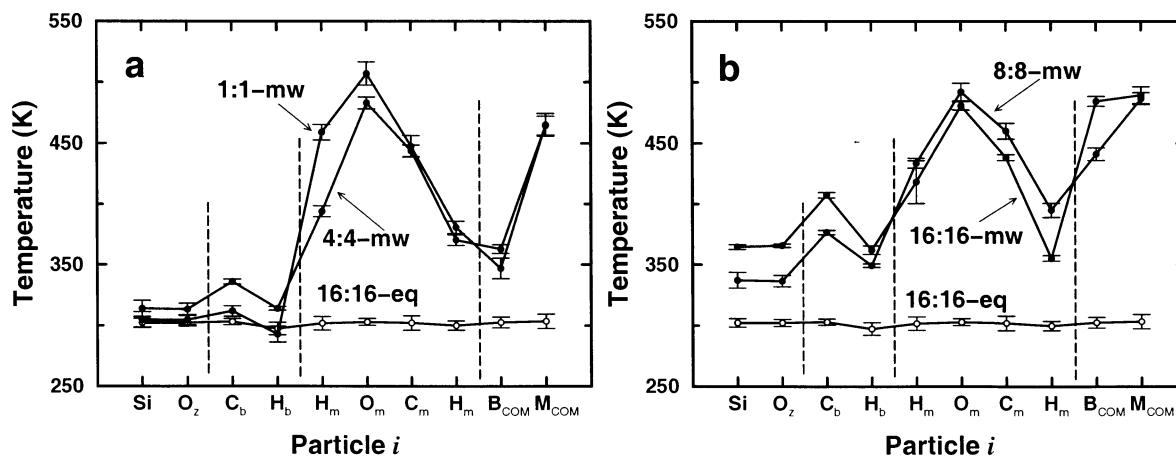


Figure 8. Energy distributions of benzene:methanol binary mixtures in DAY ($E = 1.5 \text{ V/\AA}$ and $\tau/n = 10 \text{ fs/particle}$ in all MWMD runs). For comparison, both graphs (a) and (b) show equilibrium results (16:16-eq) for 16:16 benzene:methanol molecules per basic cell. In both (a) and (b), $n:n$ -mw indicates MWMD results for $n:n$ benzene:methanol per basic cell. The regions in the graphs represent (from left to right) zeolite atoms, benzene atoms, methanol atoms, and centers-of-mass of benzene and methanol, respectively.

MWMD of 16:16 benzene:methanol in silicalite shows that energy transfer between benzene and methanol is more facile than that at lower loadings in this system, with steady-state temperatures of 425 ± 15 and $450 \pm 10 \text{ K}$ for benzene and methanol, respectively. At this highest loading, benzenes are forced to occupy channels alongside methanol molecules, hence facilitating energy transfer.

We find it interesting that for 16:16 benzene:methanol in DAY, center-of-mass thermalization between the two guest phases is essentially complete; while for 16:16 benzene:methanol in silicalite, this thermalization is still incomplete. One might expect the opposite, because 16:16 benzene:methanol in silicalite is more tightly packed than that in DAY. One possible explanation is that the MFI channel structure allows for quasi-one-dimensional energy transfer complexes, while FAU supercages allow for fully three-dimensional communication of energy. More work is needed to understand the precise mechanisms of thermalization in these MW-driven zeolite-guest systems.

IV. Summary and Concluding Remarks

We have performed equilibrium MD- and MW-driven MD (MWMD) simulations to study heating of zeolites and zeolite-guest systems with either conventional heat or MW radiation, motivated by recent MW sorption studies by Turner et al.² The purpose of our study is to determine how energy is distributed in MW-driven zeolite-guest systems as compared with isothermal systems, and how these energy distributions are influenced by the loading of guest molecules inside the zeolite. We paid particular attention to using thermostats in MWMD to produce experimentally relevant steady states. We studied the MW heating of zeolites with different Si:Al ratios and topologies: NaY, DAY, and silicalite. We then performed MWMD simulations on zeolite-guest systems with benzene and/or methanol in silicalite or DAY. In general, we found a variety of circumstances under which athermal energy distributions can be produced. We also identified mechanisms through which these athermal energy distributions might appear thermalized under certain experimental conditions.

We found that the siliceous zeolites, DAY and silicalite, exhibit relatively little MW heating, while NaY gives much stronger MW heating because of its relatively mobile Na cations. We observed that MWMD with the Andersen thermostat gives robust steady states, while MWMD with the Nosé-Hoover

chain thermostat suffers from instability. MW-driven steady states for NaY revealed that Na cations remain much hotter than the zeolite framework, indicating the possibility of strongly athermal energy distributions. Relaxation simulations on NaY reached equilibrium on picosecond time scales, indicating that suitable MW duty cycles can thermalize these nonequilibrium energy distributions.

Our MWMD simulations of guests in DAY or silicalite show minimal MW heating in zeolite-benzene systems, but also show significant MW heating in zeolite-methanol systems, with steady-state temperatures increasing linearly with methanol loading. MWMD simulations on equimolar mixtures of benzene and methanol in DAY or silicalite exhibit two interesting regimes. For low to medium loadings of benzene and methanol, up to one molecule each of benzene and methanol per cage, we found statistically different temperatures for each component, satisfying $T_{\text{methanol}} \gg T_{\text{benzene}} > T_{\text{zeolite}}$. This result is remarkable because thermalization might be expected from intracage benzene-methanol interactions. Our results predict that, at this loading, such interactions are too weak to thermalize the benzene and methanol phases. However, at twice this loading (two molecules each of benzene and methanol per cage), we found $T_{\text{methanol}} \sim T_{\text{benzene}} > T_{\text{zeolite}}$, suggesting that closely related MW sorption studies can produce markedly different results viz. athermal effects.

We thus predict that MW heating of binary mixtures in zeolites can produce effects that are qualitatively different from those obtained with conventional heating. Heating an equilibrium binary mixture of methanol and cyclohexane in DAY would desorb more cyclohexane because of its higher heat of adsorption. However, MW heating the same system, leading to the energy distribution in Figure 8b 8:8-mw, would desorb more methanol because of its higher dipole moment. Our simulations have thus provided the first atomistically detailed picture of MW-driven zeolite-guest systems. By examining how MWs and effluent gases conspire to create novel energy distributions between a zeolite and its guests, we have a first glimpse how nonequilibrium adsorption can be tailored to provide novel and possibly energy-efficient separations.

In future work, we will consider other thermostats, explicit He collisions, and the relevant energy balances between system and thermostat. We will also explore how relaxation dynamics are influenced by cation-frame, zeolite-guest, and guest-guest energy transfer processes. Finally, we will address whether such

athermal conditions and reversed desorption selectivities persist for mixtures flowing through zeolite membranes.

Acknowledgment. We thank Prof. Curtis Conner and Dr. Michael Turner for stimulating discussions regarding their microwave sorption experiments. We also thank Dr. Chris Mundy for help in testing our Nosé–Hoover code. We acknowledge generous funding from the National Science Foundation CAREER Program (NSF CTS-9734153), and from the UMass Amherst Department of Chemistry for computational resources. S.M.A. is a Sloan Foundation Fellow and a Camille Dreyfus Teacher-Scholar.

Supporting Information Available: Structure, charge, and IR analysis of methanol. This material is available free of charge via the Internet at <http://pubs.acs.org>.

References and Notes

- van Bekkum, H.; Flanigen, E. M.; Jansen, J. C., Eds. *Introduction to Zeolite Science and Practice*; Elsevier: Amsterdam, 1991.
- Turner, M. D.; Laurence, R. L.; Conner, W. C.; Yngvesson, K. S. *J. AICHE* **2000**, *46*, 758.
- Kobayashi, S.; Kim, Y.-K.; Kenmizaki, C.; Kushiya, S.; Mizuno, K. *Chem. Lett.* **1996**, *9*, 769.
- Lopes, J. M.; Serralha, F. N.; Costa, C.; Lemos, F.; Ribeiro, R. *Catal. Lett.* **1998**, *53*, 103.
- Hajek, M.; *Collect. Czech. Chem. Commun.* **1996**, *62*, 347.
- Marun, C.; Conde, L. D.; Suib, S. L. *J. Phys. Chem. A* **1999**, *103*, 4332.
- Mintova, S.; Mo, S.; Bein, T. *Chem. Mater.* **1998**, *10*, 4030.
- Cundy, C. S. *Collect. Czech. Chem. Commun.* **1998**, *63*, 1699.
- Rao, K. J.; Vaidyanathan, B.; Ganguli, M.; Ramakrishnan, P. A. *Chem. Mater.* **1999**, *11*, 882.
- Peelamedu, R. D.; Roy, R.; Agrawal, D. K. *J. Mater. Res.* **2001**, *344*, 2770.
- Peelamedu, R. D.; Roy, R.; Agrawal, D. *Mater. Res. Bull.* **2001**, *36*, 2723.
- Pozar, D. M. *Microwave Engineering*, 2nd.; John Wiley & Sons: New York, 1998.
- Stuerga, D. A. C.; Gaillard, P. J. *Microwave Power Electromagn. Energy* **1996**, *31*, 87.
- Stuerga, D. A. C.; Gaillard, P. J. *Microwave Power Electromagn. Energy* **1996**, *31*, 101.
- Blanco, C.; Auerbach, S. M. *J. Am. Chem. Soc.* **2002**, *124*, 6250.
- Allen, M. F.; Tildesley, D. J. *Computer Simulation of Liquids*; Oxford Science Publications: Oxford, 1987.
- Frenkel, D.; Smit, B. *Understanding Molecular Simulations*; Academic Press: San Diego, 1996.
- Levine, R. D.; Bernstein, R. B. *Molecular Reaction Dynamics and Chemical Reactivity*; Oxford University Press: New York, 1987.
- Jentys, A.; Grimes, R. W.; Gale, J. D.; Catlow, R. A. *J. Phys. Chem.* **1993**, *97*, 13535.
- Auerbach, S. M.; *Int. Rev. Phys. Chem.* **2000**, *19*, 155.
- Jaramillo, E.; Auerbach, S. M. *J. Phys. Chem. B* **1999**, *103*, 9589.
- Auerbach, S. M.; Henson, N. J.; Cheetham, A. K.; Metiu, H. I. *J. Phys. Chem.* **1995**, *99*, 10600.
- Jaramillo, E.; Grey, C. L.; Auerbach, S. M. *J. Phys. Chem. B* **2001**, *105*, 12319.
- Jousse, F.; Auerbach, S. M.; Vercauteren, D. P. *J. Phys. Chem. B* **2000**, *104*, 2360.
- Fitch, A. N.; Jobic, H.; Renouprez, A. *J. Phys. Chem.* **1986**, *90*, 1311.
- Kärger, J.; Ruthven, D. M. *Diffusion in Zeolites and Other Microporous Solids*; John Wiley & Sons: New York, 1992.
- Demontis, P.; Yashonath, S.; Klein, M. L. *J. Phys. Chem.* **1989**, *93*, 5016.
- Ayappa, K. G.; *Rev. Chem. Eng.* **1997**, *13*, 1.
- Whittington, B. I.; Milestone, N. B. *Zeolites* **1992**, *12*, 815.
- Hriljac, J. A.; Eddy, M. M.; Cheetham, A. K.; Donohue, J. A.; Ray, G. J. *J. Solid State Chem.* **1993**, *106*, 66.
- van Koningsveld, H.; van Bekkum, H.; Jansen, J. C. *Acta Crystallogr. B* **1987**, *43*, 127.
- Gupta, A.; Clark, L. A.; Snurr, R. Q. *Langmuir* **2000**, *16*, 3910.
- Discover 2.9.7/95.0/3.0.0 User Guide*; Biosym/MSI: San Diego, 1995.
- Jackson, J. D. *Classical Electrodynamics*; Wiley: New York, 1975.
- Bull, L. M.; Henson, N. J.; Cheetham, A. K.; Newsam, J. M.; Heyes, S. J. *J. Phys. Chem.* **1993**, *97*, 11776.
- Gale, J. D.; Catlow, C. R. A.; Carruthers, J. R. *Chem. Phys. Lett.* **1993**, *216*, 155.
- Allinger, N. L.; Rahman, M.; Lii, J.-H. *J. Am. Chem. Soc.* **1990**, *112*, 8293.
- Lees, R. M.; Baker, J. G. *J. Chem. Phys.* **1968**, *48*, 5299.
- Frisch, M. J.; Trucks, G. W.; Schlegel, H. B.; Scuseria, G. E.; Robb, M. A.; Cheeseman, J. R.; Zakrzewski, V. G.; Montgomery, J. A., Jr.; Stratmann, R. E.; Burant, J. C.; Dapprich, S.; Millam, J. M.; Daniels, A. D.; Kudin, K. N.; Strain, M. C.; Farkas, O.; Tomasi, J.; Barone, V.; Cossi, M.; Cammi, R.; Mennucci, B.; Pomelli, C.; Adamo, C.; Clifford, S.; Ochterski, J.; Petersson, G. A.; Ayala, P. Y.; Cui, Q.; Morokuma, K.; Malick, D. K.; Rabuck, A. D.; Raghavachari, K.; Foresman, J. B.; Cioslowski, J.; Ortiz, J. V.; Stefanov, B. B.; Liu, G.; Liashenko, A.; Piskorz, P.; Komaromi, I.; Gomperts, R.; Martin, R. L.; Fox, D. J.; Keith, T.; Al-Laham, M. A.; Peng, C. Y.; Nanayakkara, A.; Gonzalez, C.; Challacombe, M.; Gill, P. M. W.; Johnson, B. G.; Chen, W.; Wong, M. W.; Andres, J. L.; Head-Gordon, M.; Replogle, E. S.; Pople, J. A. *Gaussian98*, revision A.3; Gaussian, Inc.: Pittsburgh, PA, 1998.
- Szabo, A.; Ostlund, N. S. *Modern Quantum Chemistry: Introduction to Advanced Electronic Structure Theory*; McGraw-Hill: New York, 1989.
- Serrallach, A.; Meyer, R.; Gunthard, H. H. *J. Mol. Spectrosc.* **1974**, *52*, 94.
- Kimura, K.; Kubo, M. *J. Chem. Phys.* **1959**, *30*, 151.
- Ivash, E. V.; Dennison, D. M. *J. Chem. Phys.* **1953**, *21*, 1804.
- Nayak, V. S.; Moffat, J. B. *J. Phys. Chem.* **1988**, *92*, 7097.
- Thamm, H. *J. Chem. Soc., Faraday Trans. 1* **1989**, *85*, 1.
- Pope, C. G.; *J. Chem. Soc., Faraday Trans. 1* **1993**, *89*, 1139.
- Izmailova, S. G.; Karetina, J. V.; Khvoshchev, S. S.; Shubaeva, M. A. *J. Colloid Interface Sci.* **1994**, *165*, 318.
- Caro, J. et al. *J. Chem. Soc., Faraday Trans. 1* **1987**, *83*, 1843.
- Henson, N. J. Ph.D. Thesis, Oxford University, Oxford, 1996.
- Nosé, S. *J. Chem. Phys.* **1984**, *81*, 511.
- Hoover, W. G. *Phys. Rev. A* **1985**, *31*, 1695.
- Martyna, G. J.; Klei, M. L.; Tuckerman, M. E. *J. Chem. Phys.* **1992**, *97*, 2635.
- Jang, S.; Voth, G. A. *J. Chem. Phys.* **1997**, *107*, 9514.
- Jang, S.; Voth, G. A. *J. Chem. Phys.* **1999**, *110*, 3626.
- Bohm, D.; Gross, E. P. *Phys. Rev.* **1949**, *75*, 1864.
- Dellago, C.; Bolhuis, P. G.; Csajka, F. S.; Chandler, D. *J. Chem. Phys.* **1998**, *108*, 1964.
- Andersen, H. C. *J. Chem. Phys.* **1980**, *72*, 2384.
- Jousse, F.; Vercauteren, D. P.; Auerbach, S. M. *J. Phys. Chem. B* **2000**, *104*, 8768.
- Chandler, D. *Introduction to Modern Statistical Mechanics*; Oxford University Press: New York, 1987.
- Vlad, M. O.; Ross, J. *J. Chem. Phys.* **1994**, *100*, 7295.
- Eyink, G. L.; Lebowitz, J. L.; Spohn, H. *J. Stat. Phys.* **1996**, *83*, 385.
- Tuckerman, M. E.; Mundy, C. J.; Klein, M. L. *Phys. Rev. Lett.* **1997**, *78*, 2042.
- Hoover, W. G.; Evans, D. J.; Posch, H. A.; Holian, B. L.; Morriss, G. P. *Phys. Rev. Lett.* **1998**, *80*, 4103.
- Sitenko, A. G. *Phys. Lett. A* **1999**, *252*, 336.
- Jobic, H.; Smirnov, K. S.; Bougeard, D. *Chem. Phys. Lett.* **2001**, *344*, 147.
- Smirnov, K. S.; Bougeard, D. *Catal. Today* **2001**, *70*, 243.
- Jousse, F.; Auerbach, S. M.; Jobic, H.; Vercauteren, D. P. *J. Phys. IV France* **2000**, *10*, 147.